Long wavelength infrared imaging under ambient thermal radiation via an all-silicon metalens

LUOCHENG HUANG,[1] ZACHARY COPPENS,[2] KENT HALLMAN,[3] ZHEYI HAN,[1] KARL F. BÖHRINGER,[1] NESET AKOZBEK,[3] ASHOK RAMAN,[2] AND ARKA MAJUMDAR[1,4,*]

[1] *Department of Electrical Engineering, University of Washington, Seattle, WA 98195, USA*
[2] *CFD Research Corporation, Huntsville, AL 35806, USA*
[3] *BlueHalo Corporation, Huntsville, AL 35806, USA*
[4] *Department of Physics, University of Washington, Seattle, WA 98195, USA*
*arka@uw.edu

Abstract: Further miniaturization of imaging systems is prevented by the prevalent, traditional bulky refractive optics today. Meta-optics have recently generated great interest in the visible wavelength as a replacement for refractive optics thanks to their low weight, small size, and amenability to high-throughput semiconductor manufacturing. Here, we extend these meta-optics to the long-wave infrared (LWIR) regime and demonstrate imaging with a 2 cm aperture *f*/1 all-silicon metalens under ambient thermal emission. We showed that even with the strongly chromatic nature of the metalenses, we can perform ambient light imaging, primarily due to the lack of wavelength discrimination in the sensor, as is the norm for an RGB-camera in the visible.

1. Introduction

Long-wavelength infrared (LWIR) imaging is a critical technology to defense and national security, condition monitoring, medical imaging, and non-contact thermography [1–3]. Many of these applications, including wearables and autonomous drone surveillance, impose stringent criteria on size, weight and power (SWaP), and it is imperative to find solutions to create miniature LWIR imaging devices. However, it is difficult to miniaturize LWIR optics using the traditional refractive optics due to their volumetric nature. A refractive optical element relies on the precise surface curvature of the dielectric to bend the incident light and requires a large total thickness and added weight to accommodate high numerical aperture (NA) applications. One way to reduce the size of the LWIR optics is to use diffractive optical elements (DOE) such as a multilevel diffractive lens (MDL) [4]. Rather than introducing a continuous phase shift via varying the dielectric material thickness, MDL wraps the phase and only uses just enough Sagittal depth to cover the 0-2π phase shift. Though an effective way to reduce the overall thickness of the optic element, MDLs have several drawbacks in the complexity of the multi-layer fabrication. Additionally, MDLs generally have large periodicity resulting in higher order diffraction.

Sub-wavelength diffractive optics, also known as meta-optics have recently generated strong interest. A meta-optic employs a library of scatterers that can abruptly modulate the phase, amplitude, and polarization of the incident wavefront. These scatterers sit on a sub-wavelength periodic lattice to avoid any higher order diffraction [5–17]. The sub-wavelength periodicity also enables different phase-shifts for the same thickness, with different lateral geometries of the scatterers. This allows fabricating meta-optics with a single stage lithography, considerably reducing the fabrication complexity. While meta-optics allow the creation of ultra-thin flat optics, they generally suffer from strong chromatic aberration. This prevents them from capturing high quality visible images using color (RGB) cameras. Dispersion engineered metalenses have been

used in the past to capture full-color images, albeit with smaller apertures [15,18–22]. Full-color imaging with larger aperture meta-optics can be captured exploiting computational imaging [23–25].

A similar endeavor in LWIR wavelength range using meta-optics is lacking. Recently, imaging under laser illumination has been demonstrated in the LWIR regime [17]. Broadband imaging under ambient light has also been recently demonstrated using MDL [26]. Here we test the broadband imaging capability of all-silicon LWIR metalens. We design, fabricate, and characterize our meta-optics with an NA of 0.45 and a diameter of 2 cm. The performance of the metalens is tested in mixed temperature environments (to emulate different wavelengths) such as ambient, hot, and cold conditions yet the proposed system has maintained good imaging quality throughout. As the detectors in the LWIR range do not have any color filters, and we do not often require aesthetically pleasing images, even a simple, chromatic metalens can provide acceptable imaging under ambient light.

2. Methods

2.1. Design

To simplify the fabrication process, we choose silicon as the material for the meta-optics. Specifically, our meta-atoms are square silicon posts created by partially etching a silicon wafer. We note that, while silicon is slightly absorptive in the LWIR range, we still expect $\sim 80\%$ of the light to be transmitted. The metalens is designed by placing appropriate scatterers in a square lattice. The schematic of a unit cell of the nanopost is shown on Fig. 1(a). By adjusting the widths of these square nanoposts, we can modify the effective index of the nanoposts and thus change the transmission coefficient (both amplitude and phase) of the incident light. We perform rigorous coupled-wave analysis (RCWA) to map the nanopost width to the respective transmission coefficient [27], shown on Fig. 1(b). To account for the variable etch-depth, we calculate the amplitude and phase responses of posts with heights deviating by $\pm 100 nm$ from the desired thickness. We find that there is little change in the phase-values, making the scatterers robust to fabrication imperfections. Note that the resonances occur at some geometries where the amplitude takes a large dip, shown on the gray areas on 1(b). These resonances are avoided during the scatterer assignment to create the meta-optics. We assign the metalens a standard hyperboloidal phase function:

$$\phi(x, y) = \frac{2\pi}{\lambda}(\sqrt{x^2 + y^2 + f^2} - f), \tag{1}$$

where λ is the nominal wavelength set to 10 μm, and the nominal focal length f is set to 2 cm; x and y indicate the coordinates on the metalens plane. A circular aperture stop made of aluminum is added to the metalens to block stray light.

2.2. Fabrication

We start with a double side polished Si wafer with a thickness of 300 μm and p-type doping with boron giving a sheet resistivity of 1 Ω·cm to 100 Ω·cm. We first fabricate the metal aperture stop. A negative photoresist is spin-coated onto the substrate before exposed to laser direct write lithography using Heidelberg DWL 66$^+$ and development. Next, 193 nm of aluminum is evaporated via E-beam evaporator CHA SEC-600, following lift-off, creating the aluminum aperture stop. Then, a positive photoresist is spin-coated on the substrate. We then again use laser direct writing with Heidelberg DWL 66$^+$ to create the metalens pattern inside the previously defined aperture. We develop the pattern and deep reactive-ion etch 10 μm the silicon using SPTS Rapier. We note that the pillar height is controlled by the etch time, which is calibrated beforehand to approximately achieve the desired thickness of the silicon scatterer. The residual
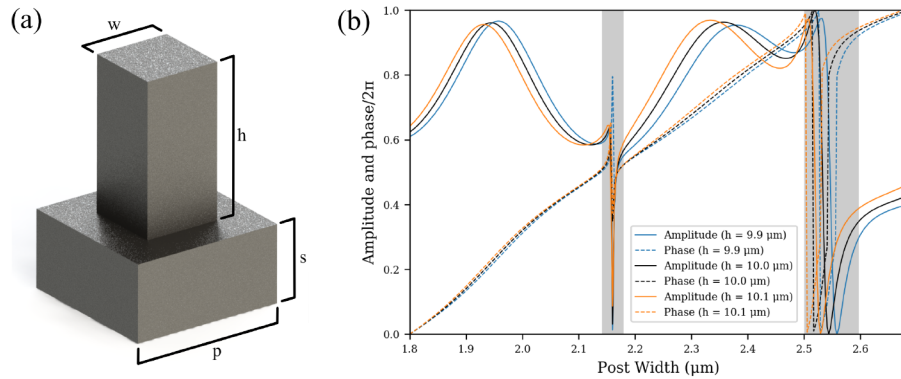
Fig. 1. (a) The geometry of the individual silicon meta-atom is shown on a silicon substrate. The height *h* of the meta-atom is 10 μm. The substrate thickness *s* is 300 μm, the periodicity of the meta-atom *p* is 4 μm. (b) The transmission coefficient as a function of the width *w* of the meta-atom, for three different thicknesses. We exclude the post widths in gray regions on the plot to ensure acceptable level of transmission. This relation is used to map between the geometry of the meta-atoms and phase distribution of the metasurface.

photoresist is subsequently stripped by oxygen plasma in YES CV200 RFS Downstream Asher. The fabricated four metasurfaces can be seen on Fig. 2(a). Scanning electron microscopy images are taken to reveal the top view (Fig. 2(b)) and a high-magnification oblique view of the metalens (Fig. 2(c)).
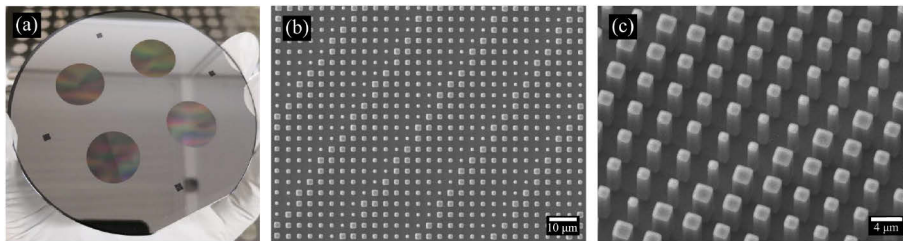

Fig. 2. Fabricated devices: (a) Image taken with a cellphone camera, (b) scanning electron microscope (SEM) images of the fabricated structures, and (c) a zoomed-in view of the device.

2.3. Characterization and imaging

The resolution and contrast of an imaging system can be estimated by measuring the modulation transfer function (MTF). The MTF signifies how the imaging system preserves the spatial frequency from the scene, and is defined as the modulus of the optical transfer function (OTF), which is the Fourier transform of the point-spread function (PSF). We simulate the PSF by propagating the pupil function of the metalens using the fast Hankel transform method for a single wavelength [28]. We note that as our metalens has a very large aperture (~2 cm), we cannot directly use angular spectrum method to propagate the wavefront [24]. The broadband OTF is the average of OTFs sampled across the sensor spectral range and weighted by the spectral radiance of the heated body at each particular wavelength. The MTFs of our imaging system under different illumination conditions but at the same sensor plane are displayed on Fig. 3(a). The MTF under narrowband illumination of 10 μm shows a near-diffraction-limited performance with a spatial cutoff frequency of $1/\lambda F$, which is strongly contrasted to that of the 12 μm source

at the same sensor plane whose cutoff frequency is nearly zero. On the other hand, the broadband sources under hot water, soldering iron, and ice temperature all perform similarly at around 80% of the diffraction-limited cutoff frequency. The spectral radiance is calculated following Planck's Law [29]:

$$B_\nu(\nu, T) = \frac{2h\nu^3}{c^2} \frac{1}{e^{h\nu/kT} - 1} \tag{2}$$

where B_ν is the spectral radiance, h is the Plank constant, c is the speed of light, k is the Boltzmann constant, ν is the wave frequency, and T is the temperature of the object. The normalized spectral radiance for different heated objects are displayed on Fig. 3(b). Thus our metalens is strongly chromatic, but due to the weighted averaging, broadband MTFs preserve much more spatial frequency components than a narrowband source, that is different from the design wavelength. This observation is not necessarily new, but should be emphasized as we can still capture images from a scene under broadband illumination using chromatic optics. Especially without having any spectral discrimination, either in the source as a transmission filter or in the detector as a color-filter, an image under broadband illumination can be captured.
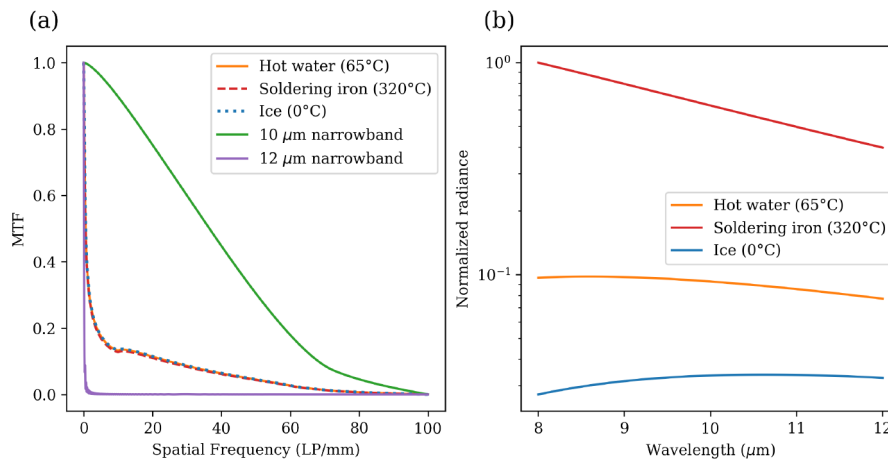

Fig. 3. (a) The simulated MTFs of the metalens under different input sources. (b) The spectra of these input sources.

The simple metalens is tested using a minimal setup shown in Fig. 4(a). On the left we have an LWIR camera mounted to an optical breadboard. The wafer is placed in front of the focal plane array at the appropriate focal distance ($f = 2cm$). We note that due to the low light from a pinhole and non-uniform noise in the LWIR detector, the measured PSF is noisy and as such does not provide much information. Hence, we characterize the metalens directly for imaging. The object distance x_o and the image distance x_i are determined by the thin lens equation $1/x_o + 1/x_i = 1/f$, where $f = 2$ cm. First, we compare LWIR imaging capabilities in the ambient environment using the isothermal background broadband imaging setup shown on the right side of Fig. 4(a). The black-body radiation source consists of a container full of water controlled at 65°C using a thermal immersion circulator. Such container is covered with electrical tape to provide an emissivity of 0.95. A steel plate with precisely machined hole diameters is placed in front of the isothermal black-body source, creating contrasting circular cutouts (Fig. 4(b)). The steel plate is placed 24 mm away from the metalens.

As shown on Fig. 4(c), the broadband imaging result using the simple metalens already creates good contrasts for the circular cutouts. To compare the performance of narrowband imaging, a bandpass filter is applied at 10 μm and 12 μm in front of the metalens, shown on Fig. 4(d) and (e), respectively. The imaging result at the designed nominal wavelength 10 μm shows better spatial
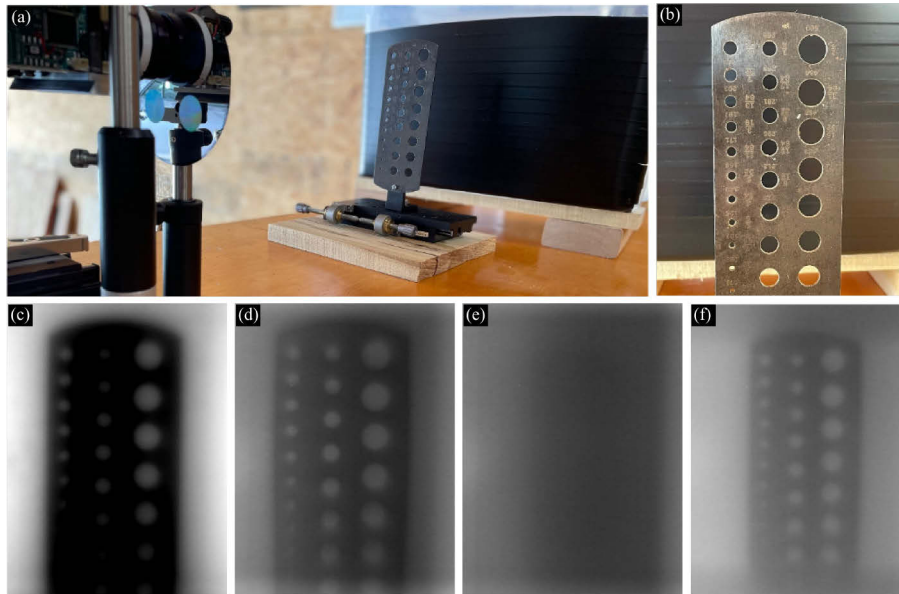
Fig. 4. (a) The LWIR imaging setup. (b) The ground truth with a steel gauge in front of an isothermal radiation source controlled at 65°C. (c) The broadband imaging result. (d) and (e) are the images when a bandpass filter centered at 10 μm and 12 μm are applied, respectively. The image is unintelligible in (e), however, when the image distance is adjusted, a clear image reappears, shown on (f).

resolution than broadband as it displays more recognizable cutouts of the metal gauge, however displaying with less contrast between the black-body background and the holey plate. This lower contrast is due to the limited number of photons in the filtered light. The imaging result at 12 μm conveys no recognizable shapes at the nominal imaging distance, however, when the metalens is moved 3 mm closer to the sensor, a clear image is formed with an imaging quality comparable to that of the 10 μm. This is expected in a metalens, where the focal length is inversely proportional to the wavelength.

The black-body radiation spectrum differs at different temperatures. To further characterize the performance of the metalens imaging system under more extreme temperatures, we include imaging of a hot soldering iron whose spectrum is shown in Fig. 3(b). The soldering iron is heated to an estimated temperature of ∼ 320°C and is mounted on an optical post in front of a steel plate covered with electrical tape with 0.95 emissivity in a garage setting seen on Fig. 5(a). It is imaged at 3.7 m away from the metalens. The imaging result on Fig. 5(d) clearly shows the hot soldering iron contrasted by the backplate, along with the sawhorse and the panels of the garage door. Next, the same soldering iron is imaged but at a closer distance of 356 mm seen on Fig. 5(b). At a closer distance, the border of the soldering iron is legible and the hot soldering iron is seen heating up a portion of the optical post assembly. To stretch the dynamic range, we include a person holding a cold ice pack and a burning blowtorch standing 3.7 m away from the metalens (Fig. 5(c)) in a garage setting. The imaging result on Fig. 5(f) clearly shows the contour of the person holding a cold item on the left with a clear border whilst the flame of the blowtorch is also visible.
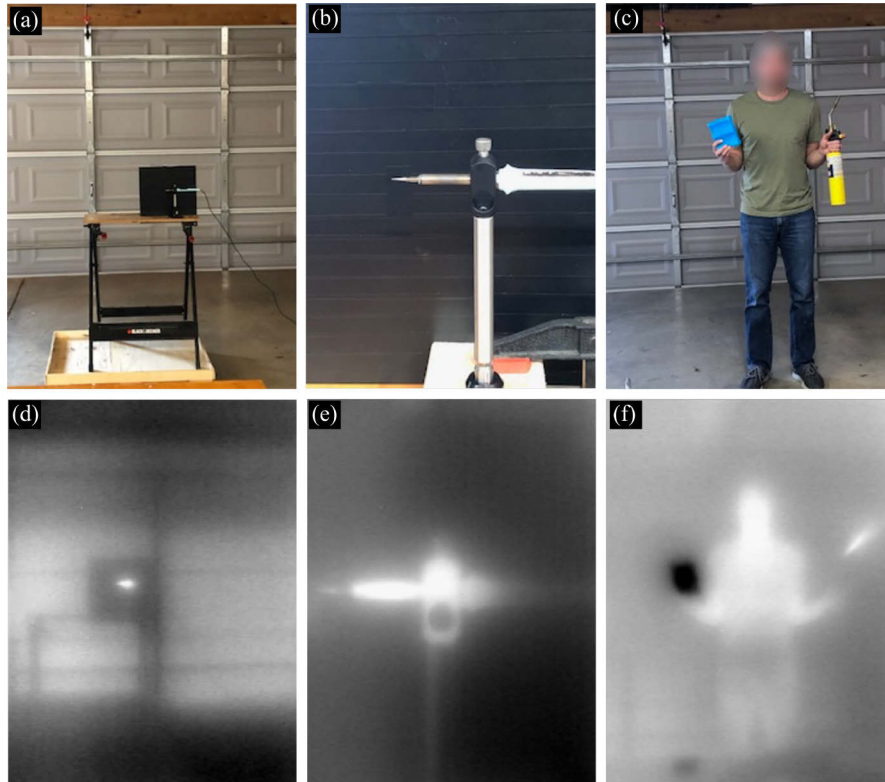
Fig. 5. A hot soldering iron is seen on (a) in front of a steel plate covered with black tape with an emissivity of 0.95. A close up image of the soldering iron on a metal holder is seen on (b). A person holding an ice pack (left) and a blowtorch (right) is seen on (c). The LWIR imaging counterparts of these images are shown on (d), (e), and (f), respectively.

3. Discussion

We are the first to demonstrate LWIR imaging using the simple metalens "in the wild", outside of the laboratory environment. Our simple metalens clearly shows a viable solution for imaging under real world ambient thermal emission applications. Here we discuss why a seemingly narrowband imaging system can be used for imaging under broadband, ambient thermal radiation. A simple metalens is known to have chromatic aberration under broadband illumination [16]: the focal length is proportional to $1/\lambda$, which is mainly caused by the discontinuities introduced by the phase-wrapping [15]. The shift in focal length across the color spectrum imparts blurs on the image. This phenomenon can be seen on Fig. 4(e) where the input wavelength is longer than the nominal wavelength and is narrowband in which case the focal length gets effectively shortened. Under narrowband and non-nominal wavelength, the MTF of the imaging system characterizes and reflects the poor imaging quality capability of this chromatically aberrated system (Fig. 3(a) purple curve), preserving very little spatial frequency.

In contrast, when imaging objects emitting black-body radiation at a variety of different temperatures, the MTFs of our imaging system drastically out-performs that of the 12 μm narrowband lighting condition, shown on Fig. 3(a). For temperatures ranging from $0 - 320°C$ the variation of the LWIR spectrum stays within an order of magnitude, seen on Fig. 3(b). This relatively uniform spectral input ensures that there is always enough signal at 10 μm. The result gives rise to a viable imaging system with a theoretical cutoff frequency of ∼ 80% of a

diffraction-limited system. We note that the imaging performance is much worse in the visible wavelengths using a color camera, as the color filters distinguish different colors. Additionally, the fractional bandwidth in the LWIR range ($\Delta\lambda/\lambda \sim 0.4$) is smaller compared to the visible range ($\Delta\lambda/\lambda \sim 0.6$).

In conclusion, we have demonstrated a simple-to-fabricate, large aperture, low f-number all silicon metasurface imaging platform capable of broadband imaging in the LWIR regime. We show that even with chromatic meta-optics, it is possible to image in the ambient light, including objects with different temperatures. This opens doors to applications such as wearable thermography devices, autonomous drones surveillance, and satellite imaging. Although we do not further process the captured images here, computational imaging combined with inverse designed meta-optics could significantly improve the overall imaging performance [25,30,31].

Disclosures. The authors declare no conflicts of interest

Data availability. Data underlying the results presented in this paper are not publicly available at this time but may be obtained from the authors upon reasonable request.

References

1. R. Schulz, S. Verstockt, J. Vermeiren, M. Loccufier, K. Stockman, and S. Van Hoecke, "Thermal imaging for monitoring rolling element bearings," in *12th International Conference on Quantitative Infrared Thermography*, Bordeaux, France, (2014), pp. 7–11.
2. E. F. J. Ring and K. Ammer, "Infrared thermal imaging in medicine," Physiol. Meas. **33**(3), R33–R46 (2012).
3. M. Vollmer and K.-P. Möllmann, *Infrared Thermal Imaging: Fundamentals, Research And Applications* (John Wiley & Sons, 2017).
4. M. Meem, S. Banerji, A. Majumder, F. G. Vasquez, B. Sensale-Rodriguez, and R. Menon, "Broadband lightweight flat lenses for long-wave infrared imaging," Proc. Natl. Acad. Sci. **116**(43), 21375–21378 (2019).
5. A. Zhan, S. Colburn, R. Trivedi, T. K. Fryett, C. M. Dodson, and A. Majumdar, "Low-contrast dielectric metasurface optics," ACS Photonics **3**(2), 209–214 (2016).
6. A. Arbabi, R. M. Briggs, Y. Horie, M. Bagheri, and A. Faraon, "Efficient dielectric metasurface collimating lenses for mid-infrared quantum cascade lasers," Opt. Express **23**(26), 33310–33317 (2015).
7. M. W. Farn, "Binary gratings with increased efficiency," Appl. Opt. **31**(22), 4453–4458 (1992).
8. F. Lu, F. G. Sedgwick, V. Karagodsky, C. Chase, and C. J. Chang-Hasnain, "Planar high-numerical-aperture low-loss focusing reflectors and lenses using subwavelength high contrast gratings," Opt. Express **18**(12), 12606–12614 (2010).
9. A. Arbabi, Y. Horie, A. J. Ball, M. Bagheri, and A. Faraon, "Subwavelength-thick lenses with high numerical apertures and large efficiency based on high-contrast transmitarrays," Nat. Commun. **6**(1), 7069 (2015).
10. D. Fattal, J. Li, Z. Peng, M. Fiorentino, and R. G. Beausoleil, "Flat dielectric grating reflectors with focusing abilities," Nat. Photonics **4**(7), 466–470 (2010).
11. F. Aieta, P. Genevet, M. A. Kats, N. Yu, R. Blanchard, Z. Gaburro, and F. Capasso, "Aberration-free ultrathin flat lenses and axicons at telecom wavelengths based on plasmonic metasurfaces," Nano Lett. **12**(9), 4932–4936 (2012).
12. M. Khorasaninejad, W. T. Chen, R. C. Devlin, J. Oh, A. Y. Zhu, and F. Capasso, "Metalenses at visible wavelengths: Diffraction-limited focusing and subwavelength resolution imaging," Science **352**(6290), 1190–1194 (2016).
13. S. Banerji, M. Meem, A. Majumder, B. Sensale-Rodriguez, and R. Menon, "Extreme-depth-of-focus imaging with a flat lens," Optica **7**(3), 214–217 (2020).
14. E. Arbabi, A. Arbabi, S. M. Kamali, Y. Horie, and A. Faraon, "Multiwavelength polarization-insensitive lenses based on dielectric metasurfaces with meta-molecules," Optica **3**(6), 628–633 (2016).
15. E. Arbabi, A. Arbabi, S. M. Kamali, Y. Horie, and A. Faraon, "Controlling the sign of chromatic dispersion in diffractive optics with dielectric metasurfaces," Optica **4**(6), 625–632 (2017).
16. S. Colburn, A. Zhan, and A. Majumdar, "Metasurface optics for full-color computational imaging," Sci. Adv. **4**(2), eaar2114 (2018).
17. Q. Fan, M. Liu, C. Yang, L. Yu, F. Yan, and T. Xu, "A high numerical aperture, polarization-insensitive metalens for long-wavelength infrared imaging," Appl. Phys. Lett. **113**(20), 201104 (2018).
18. M. Khorasaninejad, Z. Shi, A. Y. Zhu, W.-T. Chen, V. Sanjeev, A. Zaidi, and F. Capasso, "Achromatic metalens over 60 nm bandwidth in the visible and metalens with reverse chromatic dispersion," Nano Lett. **17**(3), 1819–1824 (2017).

19. S. Shrestha, A. C. Overvig, M. Lu, A. Stein, and N. Yu, "Broadband achromatic dielectric metalenses," Light: Sci. Appl. **7**(1), 85 (2018).
20. W. T. Chen, A. Y. Zhu, V. Sanjeev, M. Khorasaninejad, Z. Shi, E. Lee, and F. Capasso, "A broadband achromatic metalens for focusing and imaging in the visible," Nat. Nanotechnol. **13**(3), 220–226 (2018).
21. S. Wang, P. C. Wu, V.-C. Su, Y.-C. Lai, C. H. Chu, J.-W. Chen, S.-H. Lu, J. Chen, B. Xu, C.-H. Kuan, and T. Li, "Broadband achromatic optical metasurface devices," Nat. Commun. **8**(1), 1–9 (2017).
22. W. T. Chen, A. Y. Zhu, J. Sisler, Z. Bharwani, and F. Capasso, "A broadband achromatic polarization-insensitive metalens consisting of anisotropic nanostructures," Nat. Commun. **10**(1), 1–7 (2019).
23. S. Colburn, A. Zhan, E. Bayati, J. Whitehead, A. Ryou, L. Huang, and A. Majumdar, "Broadband transparent and cmos-compatible flat optics with silicon nitride metasurfaces," Opt. Mater. Express **8**(8), 2330–2344 (2018).
24. L. Huang, J. Whitehead, S. Colburn, and A. Majumdar, "Design and analysis of extended depth of focus metalenses for achromatic computational imaging," Photonics Res. **8**(10), 1613–1623 (2020).
25. E. Tseng, S. Colburn, J. Whitehead, L. Huang, S.-H. Baek, A. Majumdar, and F. Heide, "Neural Nano-Optics for High-quality Thin Lens Imaging," arXiv e-prints arXiv:2102.11579 (2021).
26. O. Kigner, M. Meem, B. Baker, S. Banerji, P. W. Hon, B. Sensale-rodriguez, and R. Menon, "Monolithic all-silicon flat lens for broadband lwir imaging," arXiv preprint arXiv:2103.14939 (2021).
27. V. Liu and S. Fan, "S4: A free electromagnetic solver for layered periodic structures," Comput. Phys. Commun. **183**(10), 2233–2244 (2012).
28. V. Magni, G. Cerullo, and S. De Silvestri, "High-accuracy fast hankel transform for optical beam propagation," J. Opt. Soc. Am. A **9**(11), 2031–2033 (1992).
29. G. Rybicki and A. Lightman, *Radiative Processes in Astrophysics*, A Wiley-Interscience publication (Wiley, 1991).
30. Z. Lin, C. Roques-Carmes, R. Pestourie, M. Soljačić, A. Majumdar, and S. G. Johnson, "End-to-end nanophotonic inverse design for imaging and polarimetry," Nanophotonics **10**, 1177–1187 (2020).
31. E. Bayati, R. Pestourie, S. Colburn, Z. Lin, S. G. Johnson, and A. Majumdar, "Inverse designed extended depth of focus meta-optics for broadband imaging in the visible,"arXiv preprint arXiv:2105.00160 (2021).